processes

MDPI

Article

Modelling and Prediction of Fe/MWCNT Nanocomposites for Hexavalent Chromium Reduction

Zeyu Kang [1], Xiaodong Jia [1,*], Xiaolong Ma [2] and Dongsheng Wen [2,*]

[1] School of Chemical and Process Engineering, University of Leeds, Leeds LS2 9JT, UK
[2] Institute of Thermodynamics, Technical University of Munich, 85748 Garching, Germany
* Correspondence: x.jia@leeds.ac.uk (X.J.); d.wen@tum.de (D.W.)

Abstract: Chromium (Cr) is a heavy metal pollutant prevalent in freshwater resources. Current investigations into Cr(VI) removal materials primarily involve multi-component materials. Among them, iron nanoparticles and multi-walled carbon nanotubes (MWCNTs) have exhibited great promise of removal capabilities. However, determining the optimal component ratio(s) experimentally still requires a substantial amount of effort. This paper presents a novel, model-based approach which can lessen the burden by predicting the performance of new materials. The model is based on reaction kinetics equations and derives its input parameters from the size and surface area characterisations of the components, individual components removal performance, and their mixture performance at one specific component ratio. The model is validated against experimental results for Fe/MWCNT mixtures at six ratios. The root mean square error of our model is 3.95 mg/g, which is less than 3% of the total adsorption capacity, indicating that the model is reliable. The model can be used to identify the optimal component ratios of the Fe-MWCNT composite and to reveal the relationship between performance and time. To the best of our knowledge, this is the first semi-empirical model that can predict the adsorption capacity of a composite material for heavy metals. The model is founded on the generic reduction theory of adsorption, and model parameters are not tied specifically to Fe/MWCNT. Thus, it can be used for predicting the adsorption reduction properties of other multiphase materials to speed up the new material design process.

Keywords: environment remediation; heavy metal; hexavalent chromium; catalytic reduction; multi-walled carbon nanotube (MWCNT); kinetics modelling

Citation: Kang, Z.; Jia, X.; Ma, X.; Wen, D. Modelling and Prediction of Fe/MWCNT Nanocomposites for Hexavalent Chromium Reduction. *Processes* **2023**, *11*, 3271. https://doi.org/10.3390/pr11123271

Academic Editor: Fabio Carniato

Received: 31 October 2023
Revised: 19 November 2023
Accepted: 20 November 2023
Published: 22 November 2023

1. Introduction

Freshwater is a precious natural resource that is essential for human survival and development [1]. With the rapid expansion of industry, the ecology surrounding water resources has been degrading continuously [2], which causes serious environmental problems. A primary driver of this pollution is the contamination of water bodies with heavy metals [3], which poses a substantial concern due to their bioaccumulate and non-degradable nature [4]. It is now a major environmental problem that has attracted considerable research interest. Among these heavy metal contaminants, chromium (Cr) is particularly prevalent, owing to its extensive use in various metallurgical, chemical, refractory, and cast-iron processes [5]. The most common stable forms of chromium found in the environment are trivalent chromium (Cr(III)) and hexavalent chromium (Cr(VI)). Cr(III) is an essential element with low toxicity for the human body [6]. Cr(VI) is approximately one hundred times more toxic than Cr(III) and can also enter the human circulatory system through contaminated drinking water or the food chain, posing significant environmental and health risks [7].

To solve the problems above, many advanced treatment technologies and new materials have been proposed and developed for efficient Cr(VI) adsorption, from single-component materials, such as iron nanoparticles [8], iron oxide nanoparticles [9], and

adsorbents [10] to multi-component materials [11,12]. Typically, multicomponent materials consist of an adsorbent carrier and a capacity-reducing donor. Since a vast variety of materials can be used for adsorption and reduction respectively, an intensive research effort is required to determine the optimal material combinations and proportions.

Creating a model capable of predicting the heavy metal removal performance of multicomponent materials can significantly reduce the time and cost required to develop new materials. Mechanistic analysis of Cr(VI) removal is required for the development of applicable models. The majority of researchers currently analyse mechanistic data using either Langmuir and Freundlich isotherms or Pseudo-First-Order and Pseudo-Second-Order equations. However, only a small number of studies have developed predictive models based on the analysed mechanisms, which are briefly reviewed here. Mosai et al. [13] combined the geochemical modelling code PHREEQC (which stands for pH, redox, equilibrium written in the C programming language) with parameter estimation. The model was calibrated using the observed effects of pH (2–9) on the adsorption of heavy metal onto generalised weak, medium, and strong sites of agricultural soil and can predict the adsorption capacity of natural and synthetic adsorbents at various pH values. As natural clay was selected as the adsorbent in this experiment, the removal of Cr(VI) was limited to physical adsorption without any chemical reduction, and the results cannot be generalised. Based on the results of the Cr(VI) removal experiment of surfactant-modified bentonite, Castro et. al. [14] developed a model using response surface methodology, which is essentially a collection of mathematical and statistical tools useful for planning experiments, constructing models by analysing parameter interactions, and optimising processes [15]. The model can predict the adsorption capacity of Cr(VI) at various concentrations and pH values for this substance. However, as the response surface methodology is based on fitting mathematical models to existing experimental results and validating models obtained through statistical techniques [16], it cannot be used to predict a new material that has not been experimentally examined. In the meantime, several machine learning-based models for predicting the adsorption of heavy metals have been developed [17]. However, most of them are based on previously synthesised and characterised materials that have been tested for heavy metal degradation efficiency in certain environments, and these models can not predict the performance of the material in other untested environmental conditions. This is essentially a prediction of the effect of the environment on the performance of the material, rather than a prediction of the material's performance itself.

In this work, we develop a multifunctional nanocomposite by integrating the high physical adsorption capacity of a multi-walled carbon nanotube (MWCNT) [18] and the strong reducibility of iron nanoparticles (Fe) [19]. In this system, iron nanoparticles are loaded on the surface of MWCNTs, where the MWCNTs serve as adsorbents, while the iron nanoparticles act as reducing agents. Notably, the Cr(VI) removal capacity of composite material is to be shown to outperform single materials by more than four times. Based on the experimental results, we develop a predictive model derived from the reaction kinetics equation. The model parameters are derived from the size and surface area characterisations of the components, individual component removal performance, and their mixture performance at one specific component ratio. The root mean square error (RMSE) for our model is 3.95mg/g, which accounts for less than 3% of the complete adsorption capacity, thus affirming the reliability of our model. The model can be used in the following scenarios: (a) to determine the optimal component ratio or ratios; (b) to reveal the relationship between performance and time; and (c) to provide a modelling method for predicting the adsorption reduction properties of other multiphase materials. To the best of our knowledge, this is the first reaction-kinetics-based model to predict the heavy metal removal performance of unexamined new mixture materials, which shall speed up the new material design process.

2. Materials and Methods

2.1. Materials

MWCNT (>98% carbon basis, O.D. × L 6-13 nm × 2.5–20 μm) was obtained from Sigma-Aldrich (Dorset, UK). $FeCl_3 \cdot 6H_2O$ (>98%) and potassium dichromate ($K_2Cr_4O_7$, >99.5%) were bought from Scientific Laboratory Supplies (Nottingham, UK); Polyvinyl pyrrolidone (PVP) with an average M.W. of 40,000 and chromium (III) chloride hexahydrate ($CrCl_3$, >98%) from Alfa Aesar (Heysham, UK); Sodium borohydride ($NaBH_4$, >98%) from Fisher Scientific Ltd. (Loughborough, UK); and 1,5-Diphenylcarbazide (DPC, >99%) from Sigma-Aldrich (Gillingham, UK). All chemicals were used as received without further purification.

2.2. Instruments

A transmission electron microscope (TEM, FEI Tecnai TF20, Birmingham, UK) is used to observe the thickness of the $Cr(OH)_3$ and $Fe(OH)_3$ sediment layer, and the MWCNT inner diameter. The BET surface areas are tested on a Tristar 3000 (Micromeritics, Tewkesbury, UK) by analysing the adsorption pore distribution report for the MWCNT. Ultraviolet-visible spectroscopy (UV-vis) spectra of samples are measured using a UV spectrophotometer UV-1800 (Shimadzu, Milton Keynes, UK) to quantify the concentration of Cr(VI) in solutions. Sample size characterisation is investigated by dynamic light scattering (DLS) measurements using the Zetasizer Nano ZS (Malvern, Malvern, UK).

2.3. Preparation of Materials

Under magnetic stirring, 1.033 mg of 30 wt% $FeCl_3 \cdot 6H_2O$ solution is added to 50 mL of deionised water to form a $FeCl_3$ solution. After 30 min of stirring, 0.32 g of MWCNT and 2.0 g of PVP are added to the obtained $FeCl_3$ solution. Then, 40 mL of 50 mg/mL $NaBH_4$ is added dropwise and stirred overnight to reduce Fe(III) to zero-valent iron. In this phase, magnetic stirring is replaced by mechanical oscillation to prevent the magnetic field from affecting iron nanoparticles. The generated zero-valent iron nanoparticles are loaded onto the MWCNT, which serves as the support material. The final product is collected by vacuum filtration, washed with ethanol three times, dried overnight in a vacuum oven, and then stored under nitrogen protection. The single zero-valent iron nanoparticles are prepared by the same process but without MWCNTs added. Purchased MWCNTs also dealt with the same procedure but without $FeCl_3 \cdot 6H_2O$ solution added.

2.4. Cr(VI) Adsorption Capacity Analysis

The 1,5-Diphenylcarbazide (DPC) method is used to determine the Cr(VI) concentration with UV-vis spectroscopy. DPC reacts in an acid medium with Cr(VI) ions to produce a violet solution, which exhibits a characteristic peak at λ_{max} = 545 nm. As depicted in Figure 1a, the calibration curve is obtained by measuring a series of concentrations of Cr(VI) solutions reacting with the DPC solution. Figure 1b depicts a linear relationship for the Cr(VI) concentration. Consequently, $y = 37.191x - 0.0916$ with $R^2 = 0.999$, where y represents the absorption and x represents the Cr(VI) concentration. Given that the R-value is particularly close to 1, this linear equation can be used to calculate the concentration of Cr(VI) at different UV sorption values in the concentration range of 0.01–0.04 mmol/L.

15 mg of each sample is added to 34 mL of pH buffer (pH = 5.6) and dispersed by ultrasonication. Then, 6 mL of a 20 mmol/L Cr(VI) solution is added to the solution to make the initial concentration of 3 mmol/L Cr(VI). Keeping the solution under mechanical oscillation, 0.5 mL of solution is withdrawn at regular intervals and added to a bottle containing 2 mL of DPC solution and 22.5 mL of water. After 5 min, the remaining Cr(VI) concentration is determined by measuring the solution's UV absorption spectrum. The results are shown below:

As shown in Table 1, the Cr(VI) adsorption capacity of Fe/MWCNT composite is much higher than those of individual components, i.e., 5.96 and 6.75 times of those Fe and MWCNT respectively. It shall be noted that a random MCNT/Fe mass ratio of 1.5 is used in this example. However, determining the optimal ratio of each component still requires

a substantial amount of effort. A prediction model for various ratios of Fe/MWCNT composites is expected to reduce the effort.

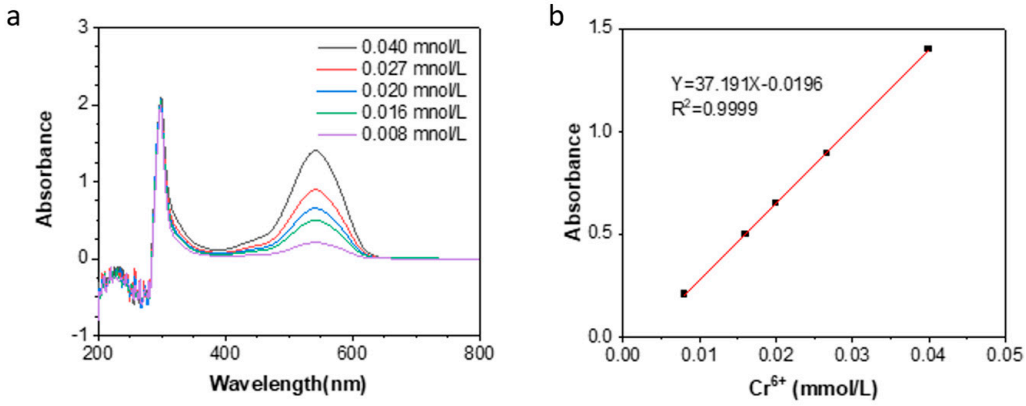

Figure 1. (**a**) UV-vis spectra of solutions of Cr(VI) reaction with DPC; (**b**) calibration curve line of Cr(VI) concentration (λ = 545 nm).

Table 1. The Cr(VI) concentration after removal test.

	pH	Adsorption Percentage	Adsorption Capacity (mg/g)	MWCNT-Fe Mass Ratio
Iron nanoparticles	5.6	5.42%	22.56	\
MWCNT	5.6	4.80%	19.95	\
Fe/MWCNT	5.6	32.35%	134.57	1.5

3. Cr(VI) Removal Mechanisms

The reduction of Cr(VI) is divided into four steps. Firstly, due to the strong physical adsorption ability of MWCNTs [20], Cr(VI) is adsorbed by MWCNTs to its surface area, increasing the concentration of Cr(VI) in the vicinity of Fe/MWCNT. Secondly, redox reactions happen between Fe(0) and Cr(III):

$$2HCrO_4^- + 14H^+ + 3Fe^0(s) \rightarrow 2Cr^{3+} + 8H_2O + 3Fe^{2+} \quad (1)$$

$$HCrO_4^- + 7H^+ + 3Fe^{2+} \rightarrow Cr(III) + 4H_2O + 3Fe^{3+} \quad (2)$$

$$Fe^0 + 2Fe^{3+} \rightarrow 3Fe^{2+} \quad (3)$$

$$Fe^0 + 2H_2O \rightarrow Fe^{2+} + H_2 + 2OH^- \quad (4)$$

In this reaction system, $HCrO_4^-$ oxidises Fe^{2+} to Fe^{3+}. At the start of the reaction, Fe(0) reduces both $HCrO_4^-$ and Fe^{3+}, with some iron undergoing several cycles of Fe^{3+} to Fe^{2+} to Fe^{3+}. Once the available Fe(0) is consumed, Fe^{3+} is no longer reduced to Fe^{2+} and only unidirectional Fe^{2+} to Fe^{3+} conversion occurs via $HCrO_4^-$ oxidation.

Previous reports have proved the generated Cr(III) and Fe(III) are in the formation of $Fe(OH)_3$ and $Cr(OH)_3$ [21–24], which are both insoluble in experiment conditions [25,26]. Figure 2 depicts Fe/MWCNT composite patterns pre- and post-removal of Cr(VI). Prior to the experiment, the Fe/MWCNT composite exhibited a sharp peak at 26.6°, corresponding to the typical (002) diffraction of MWCNTs (JCPDS No. 00–058-1638) [27]. A peak attributable to Fe(0) was observed at 44.0° (JCPDS No. 06-0696) [28]. Additionally, the inevitable oxidation of Fe(0) caused the appearance of double peaks at 33.2° and 35.5° (JCPDS No. 01-072-6225) [29]. After the experiment, the peak at 35.2° indicates the existence of $Fe(OH)_3$ (JCPDS No. 00–022-0346) [30], while the peaks at 25.8° and 62.4° point towards the presence of $Cr(OH)_3$ (JCPDS No. 00–012-0241) [31]. The absence of a clear MWCNT peak is attributed to the coverage by Fe(III) and Cr(III) hydroxides.

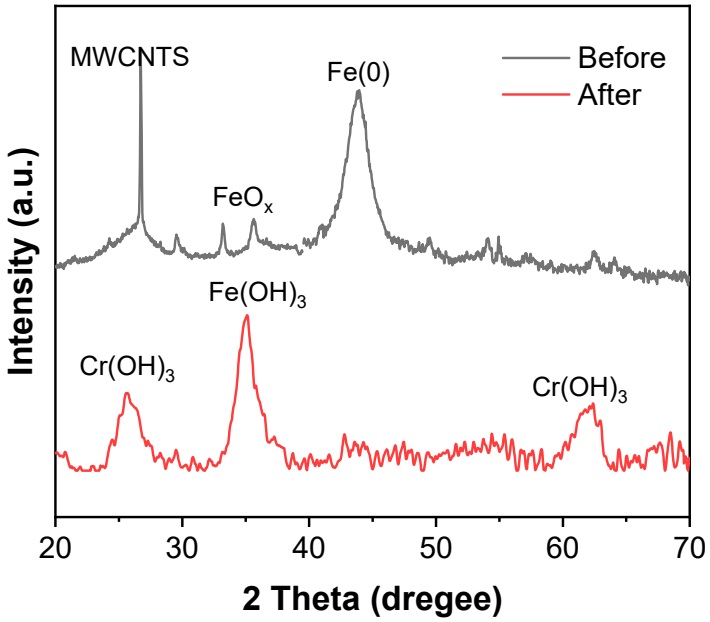

Figure 2. XRD patterns of Fe/MWCNTs composite before and after Cr(VI) removal experiment.

The above-mentioned chemical equations illustrate the molar ratio of reduced Cr(VI), generated $Cr(OH)_3$ and $Fe(OH)_3$ are 1:1:1. Thirdly, $Cr(OH)_3$ and $Fe(OH)_3$ sediments are adsorbed by the MWCNT and residual Fe(0) to form a thin layer on their surface. The layer will decrease the rate of Fe(0) reduction and MWCNT absorption. The decreased degree depends on the layer-covered area proportion. Finally, after all Fe(0) is covered or consumed, the residual MWCNT continues to adsorb Cr(VI) to its surface area until reaching the maximum absorption capacity.

Based on the above mechanism, Cr(VI) adsorption is the mix of chemical and physical reactions, traditional kinetic models are insufficient to describe it. A kinetic model is applied as follows:

$$\frac{d[Cr(VI)]}{dt} = -k[SC]_t[Cr(VI)] \tag{5}$$

where [Cr(VI)] is the Cr(VI) concentration (mmol/L) at time t, k is the rate coefficient (L $mmol^{-1}$ h^{-1}), [SC] is the equivalent sample concentration at time t that can reduce Cr(VI) (mmol L^{-1}).

Throughout the experiment, sample concentration varies over time:

$$[SC]_t = C^*_{SC}[S]\left(1 - \frac{[Cr(VI)]_0 - [Cr(VI)]_t}{C^*_{SC}[S]}\right) \tag{6}$$

where C^*_{SC} is the Cr(VI) removal capacity per gramme of sample (mmol/g) obtained from the adsorption capacity analysis experiment. [S] represents the concentration of the sample (g/L), whereas $C^*_{SC}[S]$ represents the initial concentration of [SC]. $[Cr(VI)]_0$ is the initial concentration of hexavalent chromium (mmol/L). $\frac{[Cr(VI)]_0 - [Cr(VI)]_t}{C^*_{SC}[S]}$ represents the fraction of [SC] oxidised.

Integrating the above equations results in the following:

$$[Cr(VI)]_t = \frac{[Cr(VI)]_0\{C^*_{SC}[S] - [Cr(VI)]_0\}}{C^*_{SC}[S]\exp\{k(C^*_{SC}[S] - [Cr(VI)]_0 t)\} - [Cr(VI)]_0} \tag{7}$$

where k and C^*_{SC} are the model constant parameters and t is the reaction time (min). A bespoke nonlinear fitting function in Origin was developed based on Equation (7). The function, with k and CSC* as its two variables, was used to obtain the results shown below (See Figure 3 and Table 2):

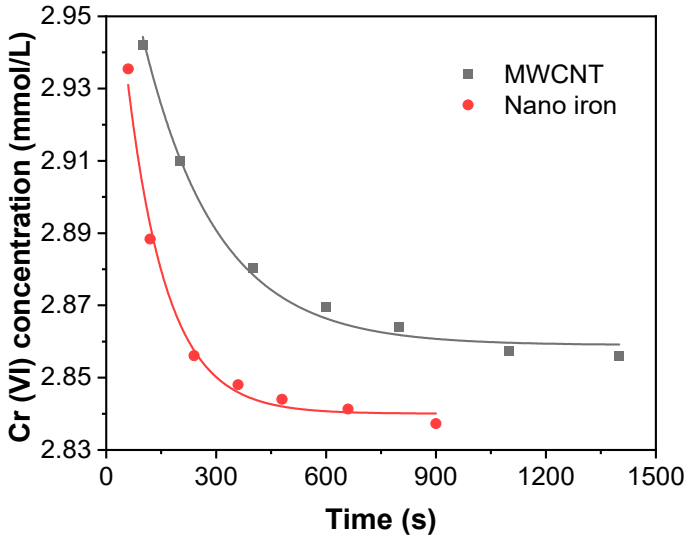

Figure 3. Cr(VI) adsorption capacity with time for MWCNT and iron. The points are independent experiment data points, lines are fitted curves.

Table 2. The kinetic model results.

	MWCNT	Iron
k (L mmol^{-1} min^{-1})	0.1014	0.1902
C^*_{SC} (mmol/g)	0.3760	0.4266
R^2-adjusted	0.9937	0.9929

The results demonstrate that the kinetic model has a high adjusted R^2 value for both MWCNT and nano iron, indicating that the model is appropriate for the Cr(VI) removal reaction. A simulation model is constructed below based on the kinetic model to predict the performance of Fe/MWCNT.

4. Modelling Mechanism and Parameter Collection

4.1. Identification and Estimation of Key Parameters

Prior to simulating the experiment, confirmation of values for some crucial parameters is needed.

4.1.1. Definition and Estimation of A_s

Here A_s is defined as the covered area of $Cr(OH)_3$ and $Fe(OH)_3$ sediment per gram of Cr(VI) reduced to Cr(III). Before and after Cr(VI) removal experiments, the sample Fe/MWCNT was characterised using a Zetasizer. A small amount of sample Fe/MWCNT powder was added to deionised water for characterisation prior to the experiment, and the measurement was conducted after sufficient ultrasonic dispersion. In order to ensure that the attached hydroxide precipitate does not fall off when characterising the sample after the Cr(VI) removal experiment, the solution used in the Cr(VI) removal experiment was used directly without additional ultrasonic dispersion. The results are shown in Figure 4.

The larger size range depicted in Figure 4 suggests that the MWCNTs were stacked disorderly. The larger size range corresponds to the MWCNTs, whereas the smaller size range diameters of 55 nm and 51 nm correspond to iron nanoparticles. According to Table 1, the Cr(VI) adsorption capacity is 134.57 mg/g. Taking into account the amount of iron nanoparticles in the sample and the Fe-Cr(VI) reaction ratio, about 31% of the iron nanoparticle weight is consumed. According to the initial average diameter and consumed amount of iron nanoparticles, the average diameter of iron nanoparticles should be 48.5 nm after Cr(VI) removal test. The difference value between 48.5 nm and 51 nm should be the thickness of $Cr(OH)_3$ and $Fe(OH)_3$ sediment, which is about 2.5 nm. To further determine

the thickness of the layer, the materials are characterised using TEM. In Figure 5, the thickness of the layer is measured to be 2.5 nm, which corresponds to the calculated data from the DLS results.

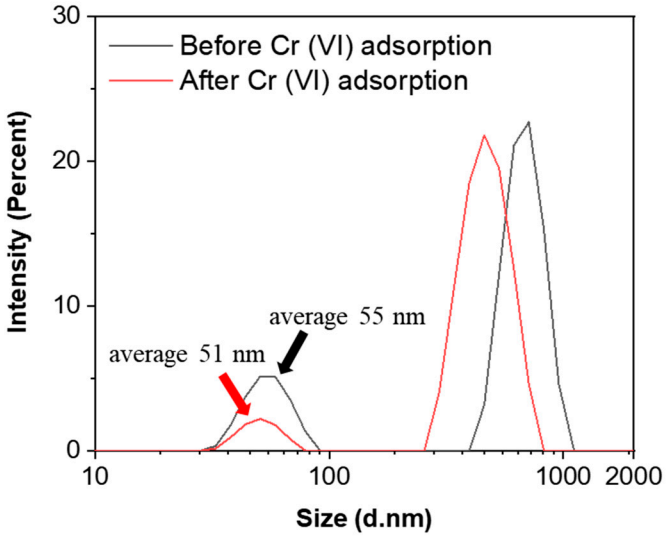

Figure 4. Zetasizer results for Fe/MWCNT.

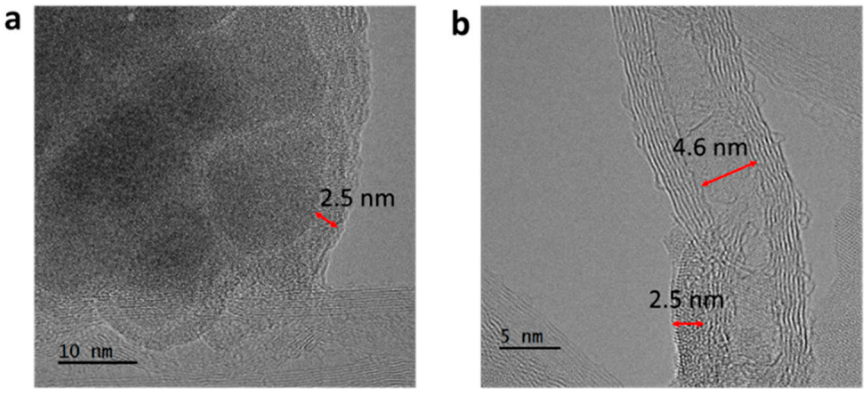

Figure 5. TEM images for iron particle (**a**) and MWCNT (**b**) after Cr(VI) degradation experiment.

The molar masses of Cr, $Cr(OH)_3$, and $Fe(OH)_3$ are 52.00 g/mol, 103.02 g/mol and 106.87 g/mol, respectively. The molar ratio of reduced Cr(VI), $Cr(OH)_3$, and $Fe(OH)_3$ are 1:1:1. The density of $Cr(OH)_3$ and $Fe(OH)_3$ are respectively 3,110,000 g/m^3 and 3,400,000 g/m^3, consequently A_s is calculated as:

$$A_s = \frac{\frac{1\ g * 103.02 \frac{g}{mol}}{52.00 \frac{g}{mol} * 3{,}110{,}000 \frac{g}{m^3}} + \frac{1\ g * 106.87 \frac{g}{mol}}{52.00 \frac{g}{mol} * 3{,}400{,}000 \frac{g}{m^3}}}{2.5\ nm} = 496.63\ m^2 \quad (8)$$

4.1.2. Specific Area for MWCNT and Iron

From Figure 4, the average diameter of an iron nanoparticle is about 55 nm. With a density of 7874 kg/m^3 and a spherical shape, the iron particle-specific surface area is approximately 13.85 m^2/g. Due to the extremely high length-to-diameter ratio, the inner area of the MWCNT is hard to competitively adsorb the $Cr(OH)_3$ and $Fe(OH)_3$ sediment with iron. Only the outer surface area of the MWCNT is active. From Figure 5, the inner diameter of the MWCNT is about 4.6 nm. By checking the diameter range in Table 3, the outer surface area for the MWCNT is about 118.494 m^2/g.

Table 3. Adsorption pore distribution report for the MWCNT.

Pore Diameter Range (nm)	Cumulative Pore Area (m^2/g)
231.8–16.3	48.889
16.3–5.9	99.711
5.9–4.6	118.494
4.6–3.6	149.244
3.6–2.6	218.081
2.6–1.8	269.389

4.2. Modelling Methodology

According to the preceding analysis, the reaction between Fe and Cr(VI) generates $Cr(OH)_3$ and $Fe(OH)_3$ precipitates, the presence of which prevented further reaction between Fe(0) and Cr(VI). Section 3 demonstrates that the reaction curves of pure Fe(0) and pure MWCNT with Cr(VI) closely match Equation (7), which is the deformation equations of Equation (5), and collects relevant fixed parameters based on Fe(0) and MWCNTs.

Section 4.1 quantified the distribution and thickness of the $Cr(OH)_3$ and $Fe(OH)_3$ precipitate adsorption layers on the surface of the MWCNT and iron particles. In Section 4.1, relevant immobilisation parameters based on Fe(0) and MWCNTs were also introduced, along with the effect of $Cr(OH)_3$ and $Fe(OH)_3$ precipitates covering Fe(0) on the reaction. The initial Cr(VI) concentration is set to 156 g/m^3.

The model is divided into two stages based on the mechanism analysis in Section 3: (1) before and (2) after iron particles have been completely encapsulated by $Cr(OH)_3$ and $Fe(OH)_3$ precipitates.

In the first stage, both MWCNTs and iron nanoparticles take part in the Cr(VI) adsorption. From Figure 3, the times for standalone MWCNTs and iron to reach the Cr(VI) adsorption equilibrium point are similar under the same conditions. However, in the Fe/MWCNT system, there is a much higher Cr(VI) concentration near iron due to the Cr(VI) being absorbed by MWCNTs. It indicates iron particles in the composite system will always arrive at the equilibrium point before the MWCNTs. As a result, the adsorption rate is dependent on the MWCNT's adsorption rate. As discussed in Section 3, the Cr(VI) adsorption rate of MWCNTs with time is described below:

$$\frac{d[Cr(VI)]}{dt} = -K_{MWCNT} C^*_{SC} [S]_t [Cr(VI)]_t \quad (9)$$

K_{MWCNTs} and C^*_{SC} values are obtained in Table 2. $[S]_t$ represents the effective surface area of the MWCNT, and can be calculated based on the following known parameters: defined effective specific surface area of iron nanoparticles and MWCNTs in Section 4.1, the covered area of $Cr(OH)_3$ and $Fe(OH)_3$ sediment per gram of Cr(VI) reduced to Cr(III): A_s (defined in Section 4.1) and the adsorbed Cr(VI) from time 0 to time t. The end time for this stage can be calculated by the unencapsulated iron nanoparticle surface area. After this time, it goes to the next stage.

In the second stage of Cr(VI) adsorption, only MWCNTs are involved. Cr(VI) is physically adsorbed by the unencapsulated surface area of the MWCNTs. The Cr(VI) adsorption rate of time is described by the same equation as stage 1. K_{MWCNTs} and C^*_{SC} values are obtained in Table 2. $[S]_t$ can be determined by integrating the amount of adsorbed Cr(VI) from time 0 to time t. In contrast to Stage 1, variation in $[S]_t$ is affected by adsorbed Cr(VI) rather than $Cr(OH)_3$ and $Fe(OH)_3$ precipitates. The details derivation process is shown below.

5. Simulation Equation Derivation

The discussion of Section 4.2 divided the overall reaction into two parts: before and after the complete encapsulation of Fe(0) by hydroxide. The mechanisms of these two parts

are fundamentally different, thus we modelled the entire process in two parts and switched the model when Fe(0) was fully encapsulated by hydroxide.

5.1. Stage 1

Prior to the complete encapsulation of iron particles by $Cr(OH)_3$ and $Fe(OH)_3$ precipitates.

$$\frac{d[Cr(VI)]_1}{dt} = -K_{MWCNT}[SC]_t[Cr(VI)]_1 \tag{10}$$

where K_{MWCNTs} is the rate coefficient (L $mmol^{-1}$ min^{-1}) of the MWCNTs, obtained from Table 2, i.e., $K_{MWCNTs} = 0.1014$ L/(mmol $*$ min). $[Cr(VI)]_1$ is the average Cr(VI) concentration for the whole bulk, excluding that adsorbed by the MWCNTs. $[SC]_t$ denotes the equivalent concentration of sample at time t. The removal compacity of Cr(VI) per unit gram of sample (mmol/g) in Equation (6) is determined as $C^*_{SC} = 0.37598$ mmol/g, based on Table 2.

B is defined as the mass ratio of the MWCNT to iron, which is a constant parameter for each sample, and $[S]_{MWCNTS}$ is the sample concentration (g/L), $[S]_{MWCNT} = \frac{15mg}{40mL} * \frac{B}{1+B}$. As $\frac{[Cr(VI)]_0 - [Cr(VI)]_t}{C^*_{SC}[S]}$ represents the fraction of [SC] oxidised. In this model, it can be defined as the fraction of MWCNT and iron-covered area, Equation (11) is derived from Equation (6):

$$[SC]_t = C^*_{SC}[S]_{MWCNT}\frac{A_{Mt}}{A_{M0}} \tag{11}$$

A_{M0} and A_{Mt} represent the exposed surface area of the MWCNT at time zero and time t, respectively. According to Section 3, the outer specific surface area of the MWCNT and the specific surface area of iron particles are 118.49 m^2/g and 13.85 m^2/g, respectively.

$$A_{M0} = 15\ mg * \frac{B}{1+B} * 118.49\frac{m^2}{g} \tag{12}$$

At time t, the ratio of uncovered MWCNT surface area and the iron area becomes $\frac{M_{MWCNT} * 118.49\ m^2/g}{M_{Fe} * 13.85\ m^2/g}$. As the reaction ratio of Fe(0) and Cr(VI) is 1:1. The molar mass of Cr and Fe are 52.00 g/mol and 55.85 g/mol, respectively. A_{Fe0} and A_{Fet} represent the exposed surface area of iron at time zero and time t, M_{Fet} represent the mass of unreacted iron. So:

$$M_{Fet} = M_{Fe} - (156\frac{g}{m^3} - Cr(VI)]_t) * \frac{55.85\frac{g}{mol}}{52.00\frac{g}{mol}} * 40\ mL \tag{13}$$

$$A_{Fe0} = 15\ mg * \frac{1}{1+B} * 13.85\frac{m^2}{g} \tag{14}$$

Expect to be covered by sediments, the total surface area of iron also decreased with the consumption of iron. At time t, the area is $A_{Fe0} * \left(\frac{M_{Fet}}{M_{Fe}}\right)^{\frac{2}{3}}$. The iron particle is assumed to always be spherical, its mass and surface area are proportional to the diameter's cube and quadratic, respectively. $\frac{2}{3}$ is the power of mass to the surface area. At time t, the MWCNT and iron adsorb the generated sediments in proportion to their total surface area.

$$A_{Mt} = A_{M0} - \int_{156}^{[Cr(VI)]_t} \left\{ \frac{A_{M0}}{A_{M0} + A_{Fe0} * \left(\frac{M_{Fet}}{M_{Fe}}\right)^{\frac{2}{3}}} * A_s * 40\ mL \right\} d[Cr(VI)]_t \tag{15}$$

$$A_{Fet} = A_{Fe0} * \left(\frac{M_{Fet}}{M_{Fe}}\right)^{\frac{2}{3}} - \int_{156}^{[Cr(VI)]_t} \left\{ \frac{A_{Fe0} * \left(\frac{M_{Fet}}{M_{Fe}}\right)^{\frac{2}{3}}}{A_{M0} + A_{Fe0} * \left(\frac{M_{Fet}}{M_{Fe}}\right)^{\frac{2}{3}}} * A_s * 40\ mL \right\} d[Cr(VI)]_t \tag{16}$$

Combined with the above equations, for Stage 1:

$$\frac{d[Cr(VI)]_1}{dt} = -K_{MWCNT} C^*_{SC} [S]_{MWCNT} \frac{A_{Mt}}{A_{M0}} [Cr(VI)]_1 \quad (17)$$

Specifically, when A_{Fet} is decreased to 0, $Cr(OH)_3$ and $Fe(OH)_3$ precipitates completely encapsulate iron particles. The reaction then advances to Stage 2.

5.2. Stage 2

After iron particles are completely encapsulated by $Cr(OH)_3$ and $Fe(OH)_3$ precipitates. Define when $A_{Fet} = 0$, $[Cr(VI)]_1 = [Cr(VI)]_s$, the time is t_s.

Equation (17) is also effective for modelling in Stage 2. Where K_{MWCNT}, C^*_{SC}, $[S]_{MWCNT}$, A_{M0} and $[Cr(VI)]_1$ are the same as Stage 1, only A_{Mt} is changed.

From Table 2, the adsorption capacity for MWCNTs is 19.95 mg/g, for per m^2 of MWCNT surface area, the adsorption amount is $\frac{19.95\frac{mg}{g} * 15\ mg * \frac{B}{B+1}}{A_{M0}}$, $([Cr(VI)]_s - [Cr(VI)]_1) * 40\ mL$ is the adsorbed Cr(VI) mass after t_s. So:

$$A_{Mt} = A_{M0} - \int_{156}^{[Cr(VI)]_s} \left\{ \frac{A_{M0}}{A_{M0} + A_{Fe0} * \left(\frac{M_{Fet}}{M_{Fe}}\right)^{\frac{2}{3}}} * A_s * 40\ mL \right\} d[Cr(VI)]_t - \frac{([Cr(VI)]_s - [Cr(VI)]_1) * 40\ mL}{\frac{19.95\frac{mg}{g} * 15\ mg * \frac{B}{B+1}}{A_{M0}}} \quad (18)$$

6. Results and Analysis

This model is implemented as a customised version of DigiDiss5ZK, a software developed by Jia [32] for the simulation of dissolution. In this model, the precipitation of $Cr(OH)_3$ following the reduction of Cr(VI) ions is regarded as the reverse process of $Cr(OH)_3$ dissolving into Cr(VI) ions. Researchers have obtained high consistency between the bespoke version of DigiDiss modelling and experimental data and demonstrated that it can be applied for predicting bulk particle dissolution [33,34]. The customised DigiDiss is capable of simulating the reaction for the Cr(VI) adsorption capacity experiment at the solid-liquid interface, based on the reaction mechanism discussed previously.

A 5 * 5 * 1 liquid phase and a 5 * 5 * 4 solid phase are imported into a 5 * 5 * 5 bulk. Pixel width is set to 0.0342 m to make the volume for one pixel 40 mL. The entire reaction is modelled in two parts: a region of uniformly distributed Cr(VI) concentrations in the solution, and a very small area of higher Cr(VI) concentrations surrounding the material. The model is designed to monitor the first part, it does not need to be nanoscale. The time step is set to 0.1 s to achieve an acceptable running time for the entire process.

Meanwhile, six various ratios of Fe/MWCNT are synthesised and evaluated for their Cr(VI) removal performance. The comparison between experimental and simulation data is presented in the table below.

Table 4 and Figure 6 demonstrate that the experimental and simulated data patterns for various MWCNT-iron ratios are comparable for all samples with iron addition. In every instance, the relative error is less than 6%. Due to the fact that not all $Cr(OH)_3$ and $Fe(OH)_3$ sediments were adsorbed by MWCNTs and iron throughout the experiment, more iron was utilised, and the adsorption capacity was increased. The experimental data consistently surpasses the simulation data by a small margin. Also, the root mean square error (RMSE) is employed to compare the modelled and experimental data. As determined by Equation (19), the RMSE for our model is 3.95 mg/g, which is less than 3% of the total adsorption capacity, indicating that the model is reliable.

$$RMSE = \sqrt{\frac{1}{N}\sum_{t=1}^{N}(experimental_t - modelling_t)^2} \quad (19)$$

Table 4. Comparison between experiment and simulation data.

	MWCNT: Fe (Weight)	Adsorption Capacity (mg/g)		Relative Error
		Experiment Data	Simulation Data	
Pure iron	0	22.56	21.6	4.26%
MWCNT	∞	19.95	19.95	0.00%
M1	0.8	116.77	111.35	4.64%
M2	1.0	122.24	119.87	1.94%
M3	1.5	134.57	132.26	1.72%
M4	2.0	140.35	137.37	2.12%
M5	3.0	140.54	136.66	2.76%
M6	5.0	125.47	121.57	3.11%
M7	8.0	101.07	95.62	5.39%

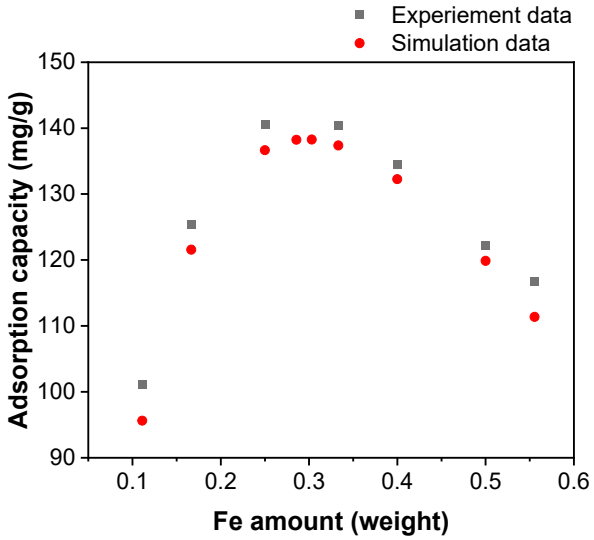

Figure 6. Comparison between experiment and simulation data.

According to modelling results, the model is in high agreement with experimental results at various Fe-MWCNT ratios and can be used to predict the performance of Fe-MWCNTs. The capacity for Cr(VI) adsorption correlates favourably with iron mass. At a weight ratio of approximately 2.33 for MWCNT to iron, the sample exhibits the highest Cr(VI) adsorption capacity. As iron weight increased, the Cr(VI) adsorption capacity increased when the ratio was less than 2.33. As iron weight increased, the Cr(VI) adsorption capacity decreased when the ratio exceeded 2.33.

In Figure 7, the line represents the simulated adsorption curve, while the points represent experimental data. This indicates that the simulated reaction rates closely match the experimentally determined rates. This indicates that the simulated reaction rate is in high agreement with the experimental results. The experimental Cr(VI) concentrations were slightly lower than the simulated concentrations at various time points. This is due to the fact that some of the hydroxides were not adsorbed by Fe and MWCNTs during the experiments, leading to faster reaction rates.

In addition, although this model has only been validated for predicting the Cr(VI) removal performance of Fe/MWCNT systems, the underlying principles are not unique to Fe and MWCNTs. Physical adsorption, redox precipitation, and precipitation attachment are also applicable to other similar reducing agents and adsorbent-based materials. Nevertheless, the Fe/MWCNT components have a simple structure and a high degree of uniformity. When similar models are applied to other materials with more components and more complex structures, it is anticipated that the model's complexity will increase significantly.

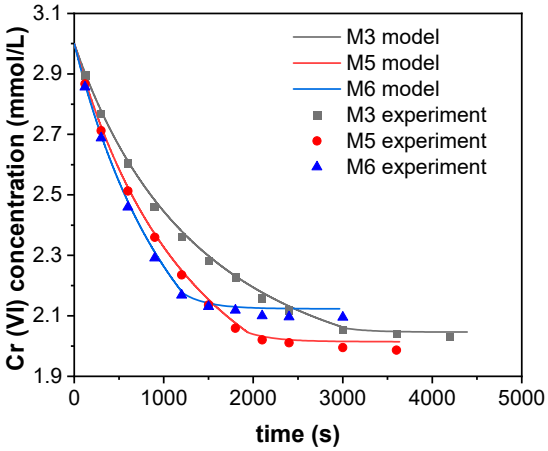

Figure 7. Comparison of adsorption curve of simulation (lines) and experiments (points).

7. Conclusions

In this study, the adsorption performance of nanocomposite particles of Fe and MWCNTs has been shown to surpass that of the individual components. To lessen the burden of determining the optimal ratio(s) of Fe/MWCNT, a semi-empirical adsorption model has been developed. The model is derived from reaction kinetics equations, and model parameters are determined from the size and surface area characterisations of the components, removal performance results for each individual component, and their mixture performance at one component ratio. The model has been validated against experimental results for Fe/MWCNT mixtures at six different ratios, and the RMSE for our model is 3.95 mg/g, which is less than 3% of the total adsorption capacity, indicating that the model is reliable. As such, the model enables the prediction of the adsorption rate of Cr(VI) at any given moment and its final adsorption capacity for any Fe/MWCNT composite ratio. To the best of our knowledge, this is the first semi-empirical model that can predict the adsorption capacity of a composite material for heavy metals. This prediction can reduce the workload for experiments. Since the model is based on the generic reduction theory of adsorption and contains no model parameters unique to Fe/MWCNT, it is expected to be able to predict the adsorption reduction properties of other multiphase materials and thus help to speed up the new material design process.

Author Contributions: Conceptualization, Z.K. and D.W.; data curation, Z.K. and X.J.; formal analysis, Z.K. and X.J.; funding acquisition, X.J. and D.W.; investigation, Z.K.; methodology, Z.K., X.J. and D.W.; project administration, X.J. and D.W.; resources, X.J. and D.W.; supervision, X.J. and D.W.; validation, Z.K., X.J. and X.M.; visualisation, Z.K. and X.J.; writing—original draft, Z.K.; writing—review and editing, Z.K., X.J., X.M. and D.W. All authors have read and agreed to the published version of the manuscript.

Funding: This research received no external funding.

Data Availability Statement: Data are contained within the article.

Acknowledgments: The authors are grateful for the support of the University of Leeds and Technical University of Munich.

Conflicts of Interest: The authors declare no conflict of interest.

References

1. Kılıç, Z. The importance of water and conscious use of water. *Int. J. Hydrol.* **2020**, *4*, 239–241. [CrossRef]
2. Qadri, R.; Faiq, M.A. Freshwater pollution: Effects on aquatic life and human health. In *Fresh Water Pollution Dynamics and Remediation*; Springer: Singapore, 2020; pp. 15–26, ISBN 978-981-13-8276-5.
3. Zamora-Ledezma, C.; Negrete-Bolagay, D.; Figueroa, F.; Zamora-Ledezma, E.; Ni, M.; Alexis, F.; Guerrero, V.H. Heavy metal water pollution: A fresh look about hazards, novel and conventional remediation methods. *Environ. Technol. Innov.* **2021**, *22*, 101504. [CrossRef]

4. Xiao, Y.; Ma, C.; Jin, Z.; Wang, J.; He, L.; Mu, X.; Song, L.; Hu, Y. Functional covalent organic framework for exceptional Fe^{2+}, Co^{2+} and Ni^{2+} removal: An upcycling strategy to achieve water decontamination and reutilization as smoke suppressant and flame retardant simultaneously. *Chem. Eng. J.* **2021**, *421*, 127837. [CrossRef]
5. Xia, S.; Song, Z.; Jeyakumar, P.; Shaheen, S.M.; Rinklebe, J.; Ok, Y.S.; Bolan, N.; Wang, H. A critical review on bioremediation technologies for *Cr*(VI)-contaminated soils and wastewater. *Crit. Rev. Environ. Sci. Technol.* **2019**, *49*, 1027–1078. [CrossRef]
6. Jiang, B.; Niu, Q.; Li, C.; Oturan, N.; Oturan, M.A. Outstanding performance of electro-Fenton process for efficient decontamination of *Cr*(III) complexes via alkaline precipitation with no accumulation of *Cr*(VI): Important roles of iron species. *Appl. Catal. B Environ.* **2020**, *272*, 119002. [CrossRef]
7. Radziemska, M.; Wyszkowski, M.; Bęś, A.; Mazur, Z.; Jeznach, J.; Brtnický, M. The applicability of compost, zeolite and calcium oxide in assisted remediation of acidic soil contaminated with *Cr*(III) and *Cr*(VI). *Environ. Sci. Pollut. Res.* **2019**, *26*, 21351–21362. [CrossRef]
8. Shao-feng, N.; Yong, L.; Xin-Hua, X.; Zhang-hua, L. Removal of hexavalent chromium from aqueous solution by iron nanoparticles. *J. Zhejiang Univ. Sci. B* **2005**, *6*, 1022–1027.
9. Lee, C.-G.; Kim, S.-B. Cr(VI) Adsorption to Magnetic Iron Oxide Nanoparticle-Multi-Walled Carbon Nanotube Adsorbents. *Water Environ. Res.* **2016**, *88*, 2111–2120. [CrossRef] [PubMed]
10. Sinha, R.; Kumar, R.; Sharma, P.; Kant, N.; Shang, J.; Aminabhavi, T.M. Removal of hexavalent chromium via biochar-based adsorbents: State-of-the-art, challenges, and future perspectives. *J. Environ. Manag.* **2022**, *317*, 115356. [CrossRef]
11. Zhang, Q.; Hou, Q.; Huang, G.; Fan, Q. Removal of heavy metals in aquatic environment by graphene oxide composites: A review. *Environ. Sci. Pollut. Res.* **2020**, *27*, 190–209. [CrossRef]
12. Gupta, V.K.; Agarwal, S.; Saleh, T.A. Chromium removal by combining the magnetic properties of iron oxide with adsorption properties of carbon nanotubes. *Water Res.* **2011**, *45*, 2207–2212. [CrossRef] [PubMed]
13. Mosai, A.K.; Tokwana, B.C.; Tutu, H. Computer simulation modelling of the simultaneous adsorption of Cd, Cu and Cr from aqueous solutions by agricultural clay soil: A PHREEQC geochemical modelling code coupled to parameter estimation (PEST) study. *Ecol. Model.* **2022**, *465*, 109872. [CrossRef]
14. Castro-Castro, J.D.; Macías-Quiroga, I.F.; Giraldo-Gómez, G.I.; Sanabria-González, N.R. Adsorption of Cr(VI) in Aqueous Solution Using a Surfactant-Modified Bentonite. *Sci. World J.* **2020**, *2020*, 3628163. [CrossRef]
15. Karimifard, S.; Alavi Moghaddam, M.R. Application of response surface methodology in physicochemical removal of dyes from wastewater: A critical review. *Sci. Total Environ.* **2018**, *640–641*, 772–797. [CrossRef]
16. Witek-Krowiak, A.; Chojnacka, K.; Podstawczyk, D.; Dawiec, A.; Pokomeda, K. Application of response surface methodology and artificial neural network methods in modelling and optimisation of biosorption process. *Bioresour. Technol.* **2014**, *160*, 150–160. [CrossRef] [PubMed]
17. Yaseen, Z.M. An insight into machine learning models era in simulating soil, water bodies and adsorption heavy metals: Review, challenges and solutions. *Chemosphere* **2021**, *277*, 130126. [CrossRef]
18. Di, Z.-C.; Ding, J.; Peng, X.-J.; Li, Y.-H.; Luan, Z.-K.; Liang, J. Chromium adsorption by aligned carbon nanotubes supported ceria nanoparticles. *Chemosphere* **2006**, *62*, 861–865. [CrossRef]
19. Xu, W.; Yang, T.; Liu, S.; Du, L.; Chen, Q.; Li, X.; Dong, J.; Zhang, Z.; Lu, S.; Gong, Y.; et al. Insights into the Synthesis, types and application of iron Nanoparticles: The overlooked significance of environmental effects. *Environ. Int.* **2022**, *158*, 106980. [CrossRef]
20. Egbosiuba, T.C.; Abdulkareem, A.S.; Kovo, A.S.; Afolabi, E.A.; Tijani, J.O.; Bankole, M.T.; Bo, S.; Roos, W.D. Adsorption of *Cr*(VI), Ni (II), Fe(II) and Cd (II) ions by KIAgNPs decorated MWCNTs in a batch and fixed bed process. *Sci. Rep.* **2021**, *11*, 75. [CrossRef]
21. Pettine, M.; D'Ottone, L.; Campanella, L.; Millero, F.J.; Passino, R. The reduction of chromium (VI) by iron (II) in aqueous solutions. *Geochim. Cosmochim. Acta* **1998**, *62*, 1509–1519. [CrossRef]
22. Butler, E.C.; Chen, L.; Hansel, C.M.; Krumholz, L.R.; Elwood Madden, A.S.; Lan, Y. Biological versus mineralogical chromium reduction: Potential for reoxidation by manganese oxide. *Environ. Sci. Process. Impacts* **2015**, *17*, 1930–1940. [CrossRef] [PubMed]
23. Joe-Wong, C.; Brown, G.E., Jr.; Maher, K. Kinetics and Products of Chromium(VI) Reduction by Iron(II/III)-Bearing Clay Minerals. *Environ. Sci. Technol.* **2017**, *51*, 9817–9825. [CrossRef]
24. Kang, Z.; Gao, H.; Ma, X.; Jia, X.; Wen, D. Fe–Ni/MWCNTs Nano-Composites for Hexavalent Chromium Reduction in Aqueous Environment. *Molecules* **2023**, *28*, 4412. [CrossRef] [PubMed]
25. Rai, D.; Sass, B.M.; Moore, D.A. Chromium(III) hydrolysis constants and solubility of chromium(III) hydroxide. *Inorg. Chem.* **1987**, *26*, 345–349. [CrossRef]
26. Stefánsson, A. Iron(III) Hydrolysis and Solubility at 25 °C. *Environ. Sci. Technol.* **2007**, *41*, 6117–6123. [CrossRef]
27. Nie, P.; Min, C.; Song, H.-J.; Chen, X.; Zhang, Z.; Zhao, K. Preparation and Tribological Properties of Polyimide/Carboxyl-Functionalized Multi-walled Carbon Nanotube Nanocomposite Films Under Seawater Lubrication. *Tribol. Lett.* **2015**, *58*, 7. [CrossRef]
28. Chen, Y.; Zhang, X.-F.; Wang, A.-J.; Zhang, Q.-L.; Huang, H.; Feng, J.-J. Ultrafine Fe_3C nanoparticles embedded in N-doped graphitic carbon sheets for simultaneous determination of ascorbic acid, dopamine, uric acid and xanthine. *Microchim. Acta* **2019**, *186*, 660. [CrossRef]
29. Li, J.; Lu, G.; Wu, G.; Mao, D.; Guo, Y.; Wang, Y.; Guo, Y. The role of iron oxide in the highly effective Fe-modified Co_3O_4 catalyst for low-temperature CO oxidation. *RSC Adv.* **2013**, *3*, 12409–12416. [CrossRef]

30. Mikhaylov, V.I. Optical and thermal properties of sol–gel $Al(OH)_3$–$Fe(OH)_3$–PVA composite films. *J. Sol-Gel Sci. Technol.* **2019**, *92*, 282–292. [CrossRef]
31. Pan, C.; Liu, H.; Catalano, J.G.; Wang, Z.; Qian, A.; Giammar, D.E. Understanding the Roles of Dissolution and Diffusion in $Cr(OH)_3$ Oxidation by δ-MnO_2. *ACS Earth Space Chem.* **2019**, *3*, 357–365. [CrossRef]
32. Jia, X.; Williams, R.A. A Hybrid Mesoscale Modelling Approach to Dissolution of Granules and Tablets. *Chem. Eng. Res. Des.* **2007**, *85*, 1027–1038. [CrossRef]
33. Cao, H. Simulations of Dissolution of Structured Particles. Ph.D. Thesis, University of Leeds, Leeds, UK, 2015.
34. Li, Y. Physics-based Simulation of Tablet Disintegration and Dissolution. Ph.D. Thesis, Purdue University Graduate School, Purdure, IN, USA, 2021.